

Modeling Quasar Photo- z Distribution and Uncertainty

A Study Based on the Kilo-Degree Survey

Kacper Drabicki¹, Szymon J. Nakoneczny^{1*}, and Maciej Bilicki¹

Center for Theoretical Physics, Polish Academy of Sciences, Al. Lotników 32/46, 02-668 Warsaw, Poland

ABSTRACT

Context. Photometric redshifts (photo- z) and their distributions are central to precision cosmology, where both predictive accuracy and reliable uncertainty quantification are crucial.

Aims. We aim to determine the most effective approach for estimating uncertainties in quasar photo- z and to evaluate the ability of different models to reconstruct the true redshift distribution under varying data quality. We use photometric magnitudes from the Kilo-Degree Survey Data Release 5 and spectroscopically confirmed quasars from the Dark Energy Spectroscopic Instrument Data Release 1.

Methods. We compare artificial neural networks (ANNs), Mixture Density Networks (MDNs), and Bayesian Neural Networks (BNNs), both latter combined with Gaussian Mixture Model (GMM) outputs. To assess robustness to observational limitations, we construct four test sets covering all combinations of (i) sources fainter than those in the training sample and (ii) missing photometric bands. We additionally apply unsupervised clustering to the predicted photo- z probability density functions to identify degenerate solutions.

Results. ANNs show substantial deviations in reconstructing the redshift distribution. MDNs require at least two Gaussian components to achieve accurate reconstruction, with the three-component MDN providing the best performance in this class. BNNs improve results for sources fainter than the training range, yielding a negative log-likelihood (NLL) gain of 0.11, but reduce performance for brighter data by 0.07 NLL. Reconstruction remains feasible for either fainter data or missing magnitudes individually; however, their combination leads to pronounced deviations. Unsupervised clustering identifies two dominant degenerate solutions at redshift pairs of (1.2, 2.3) and (1.6, 2.5).

Conclusions. Accurate uncertainty modeling is essential for reliable reconstruction of the redshift distribution directly from photo- z s. BNNs are particularly beneficial for out-of-distribution inference, although at the expense of reduced accuracy for brighter sources. Our methodology enables the identification and removal of degenerate photo- z estimates unsuitable for tomographic analyses.

Key words. Methods: data analysis – Techniques: photometric – quasars: general

1. Introduction

Photometric redshift estimates (photo- z) have become a cornerstone of modern cosmological analyses. Although they are less precise than spectroscopic measurements, photometric techniques enable redshift estimation for orders of magnitude more objects, making them indispensable for large-area surveys and statistical cosmology (e.g. Hildebrandt et al. 2010; Salvato et al. 2019; Newman & Gruen 2022). Photo- z are commonly used to construct tomographic redshift bins, which are used for cosmological inference from large-scale structure probes such as weak gravitational lensing and galaxy clustering. These distributions are often calibrated using additional data.

Beyond point estimates of redshift, cosmological analyses critically rely on a robust characterization of the associated uncertainties. Uncertainties and biases in the reconstructed redshift distribution propagate directly into systematic errors in cosmological observables that depend on accurate distance estimates. In weak gravitational lensing analyses, such errors bias the lensing efficiency kernels and can lead to incorrect constraints on parameters such as σ_8 and Ω_m . Similarly, in galaxy clustering measurements, biases in the redshift distribution affect inferred comoving distances and correlation functions, impacting both the

amplitude and scale of the signal. In this paper we focus both on individual redshift uncertainties, as well as cumulative redshift distributions, trying to reconstruct the cumulative distributions using the individual photo- z uncertainty measurements.

In case of machine learning (ML), the photo- z uncertainties are commonly decomposed into aleatoric and epistemic components. Aleatoric uncertainty arises from intrinsic degeneracies in the data, where different redshift values correspond to similar photometric colors, even in the presence of abundant training data. Epistemic uncertainty, on the other hand, is driven by incomplete coverage of the feature space by the training set, reflecting the model's lack of knowledge in poorly sampled regions.

Aleatoric uncertainty in photo- z estimation is often modeled using Mixture Density Networks (MDNs), i.e. artificial neural networks (ANNs) that parameterize the output as a Gaussian Mixture Model (GMM) (D'Isanto & Polsterer 2018; Zhang et al. 2024; Chen et al. 2025). This approach allows the prediction of full probability density functions (PDFs) rather than single-point estimates. An alternative strategy frames redshift estimation as a classification problem over discrete redshift bins (Pasquet et al. 2019). While this method avoids explicit assumptions about the functional form of the PDF, its performance and resolution are inherently limited by the chosen bin width.

* Corresponding author: S. J. Nakoneczny nakoneczny@cft.edu.pl

To capture epistemic uncertainty, Bayesian Neural Networks (BNNs) are commonly employed, in which the network weights are treated as random variables with prior distributions, typically Gaussian (Zhou et al. 2022; Jones et al. 2024). For deep neural networks, a computationally efficient approximation to full Bayesian inference is provided by Monte Carlo (MC) dropout (Luo et al. 2024). Dropout is a technique in which a subset of weights is randomly deactivated during the operation of a neural network. In the case of MC dropout, this deactivation occurs not only during training but also during inference. It therefore serves as a variational approximation to a BNN.

Here we focus on the Kilo-Degree Survey (KiDS) Data Release 5 (DR5). Within the context of KiDS, photometric redshifts (photo- z) have been estimated for both quasars and galaxies (Bilicki et al. 2021; Hildebrandt et al. 2021; Nakoneczny et al. 2021; Li et al. 2022; Vakili et al. 2023; John William et al. 2025b,a). However, a comprehensive characterization of the associated uncertainties has not yet been established.

In this work we focus exclusively on quasars. These tracers of the large-scale structure play an important role in cosmology, as they give access to much higher redshifts than regular galaxies. In the advent of the Sloan Digital Sky Survey (SDSS) and the Dark Energy Spectroscopic Instrument (DESI), the most powerful cosmological constraints using quasars are based on spectroscopic samples. Nevertheless, quasars selected photometrically continue to be useful, as such datasets are considerably more numerous and complete than what is possible with spectroscopy. Some of the recent cosmological analyses with photometric quasars cover constraints on their host halo masses (e.g. Luo et al. 2024; Eltvedt et al. 2024; John William et al. 2025a), in particular by dividing them into obscured and non-obscured (Petter et al. 2023). Quasars, or more generally active galactic nuclei, constitute an important fraction of radio-detected galaxies, hence knowing their redshift distributions is key to extract cosmological information from the largest radio samples available for instance from the Low-Frequency Array (LOFAR, e.g. Alonso et al. 2021; Nakoneczny et al. 2024). In this context, we aim to investigate how photometric redshift uncertainties can be reliably estimated for quasars and how they affect the inferred redshift distributions.

This work therefore has two main objectives. First, we aim to systematically compare photo- z uncertainty estimation using MDNs and BNNs. Such a comparison is currently lacking in the literature, particularly for quasars and in the presence of multiple sources of uncertainty such as extrapolation beyond the training set and missing photometric magnitudes. Due to the complex and degenerate spectral energy distributions of quasars, their photo- z estimates typically exhibit significantly larger uncertainties than those of galaxies, making them an ideal test case for uncertainty modeling.

The second objective is to test these machine learning models in terms of their ability to recover the original spectroscopic redshift distribution. We investigate the conditions under which a reliable reconstruction of the redshift distribution function is possible. Ultimately, this allows us to determine which models are most suitable for quasars in future cosmological analyses, for instance using the Legacy Survey of Space and Time (LSST), and how the data should be selected or trimmed in order to obtain a robust reconstruction of the redshift distribution.

To this end, we apply artificial neural networks (ANNs), MDNs, and BNNs to the problem of quasar photo- z estimation in KiDS. We design multiple test sets to probe both aleatoric and epistemic uncertainties through controlled sampling strategies. Additionally, we use unsupervised learning with the predicted

photo- z probability density functions (PDFs) to investigate degeneracies present in the training data.

This paper is organized as follows. In Section 2 we describe the KiDS data set and the construction of the training and test samples. Section 3 presents the machine learning models and the evaluation metrics used in this study. The results are discussed in Section 4, and Section 5 provides the interpretation and conclusions.

2. Data

2.1. Kilo Degree Survey

The Kilo-Degree Survey Data Release 5 (KiDS-DR5, Wright et al. 2024) is the fifth and final public release of the ESO KiDS carried out with the VLT Survey Telescope and the OmegaCAM instrument. DR5 provides deep, homogeneous optical imaging over approximately 1347 deg^2 in the u, g, r, i broadband filters, with two independent epochs in the i -band. The data reach a typical 5σ limiting magnitude of $r \simeq 24.8$ AB mag, with median seeing of about $0.7''$, enabling the detection of faint extragalactic sources and accurate shape measurements for weak-lensing analyses. When combined with near-infrared photometry from the VIKING survey (Edge et al. 2013), KiDS-DR5 delivers multi-band $ugriZYJHK_s$ catalogs suitable for a wide range of cosmological and astrophysical applications (Wright et al. 2024).

2.2. Preprocessing

We cross-match KiDS DR5 with quasars from the Dark Energy Spectroscopic Instrument (DESI, DESI Collaboration et al. 2016) Data Release 1 (DR1, DESI Collaboration et al. 2025) within 1 arcsec radius. We clean KiDS by applying the condition $\text{MASK} < 2$. The DESI quasars were selected according to $\text{SPECTYPE} = \text{'QSO'}$ and with $\text{ZWARN} = 0$ to remove objects flagged with redshift warning. The data consists of 124638 quasars.

3. Methodology

3.1. Features

Our initial feature space comprised GAAP magnitudes (Kuijken 2008; Kuijken et al. 2015, 2019) in 10 photometric bands - $u, g, r, i1, i2, Z, Y, J, H,$ and K_s - which served as the primary inputs for quasar photo- z estimation. We perform basic feature engineering by calculating magnitudes differences (colors). The resulting feature space comprises 55 dimensions. We also tested adding magnitude errors to the feature set; however, none of the experiments showed any improvement in performance.

3.2. Test sets

The overall sample has a median r -band magnitude of 21.5 and a 90th percentile of 22.9. To examine the extrapolation performance of the models, we defined a faint-extrapolation subset by selecting the top 10% of objects ($r > 22.9$) with the faintest r -band magnitudes. After removing these objects from the main sample, we split the remaining data into training, validation, and test subsets in an 8:1:1 ratio. We hereafter refer to this test subset as the random test set.

Approximately 3.5% of the objects lack at least one feature. Among these, the vast majority (88%) are missing only

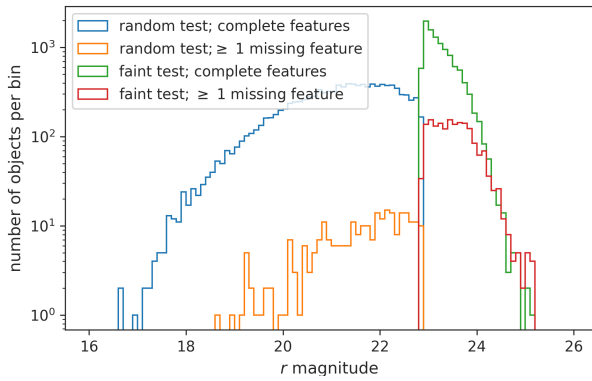


Fig. 1. Distributions of test sets over r magnitude. The faint-extrapolation test set includes the top 10% of r values, starting at $r > 22.9$. The random test contains a randomly selected 10% of the objects with $r < 22.9$. Both test sets are comparable in size. The faint-extrapolation set appears more prominent only because its objects are concentrated in a much narrower r range, whereas the random set is spread widely. We further split the both test sets into subsets with complete features and at least one missing feature.

a single magnitude. The most frequent gap is observed in the u band, which accounts for 76% of all incomplete cases, and is also one of the most important magnitudes for QSO photo- z (Nakoneczny et al. 2021). We address these cases by replacing each missing entry with the maximum value of that feature in the training subset, hence, outside the faint-extrapolation subset; we use these same values to impute missing features in the faint-extrapolation subset for consistency. We then divide the random and the faint-extrapolation test sets into four groups: (i) objects with complete features in random-test; (ii) objects with complete features in extrapolation-test; (iii) objects with at least one missing feature in random-test; and (iv) objects with at least one missing feature in extrapolation-test. Figure 1 shows the distribution of r -band magnitudes in each of these four subsets.

3.3. Artificial neural networks

We test three model families: a fully connected artificial neural network (ANN); Mixture Density Network (MDN) with Gaussian-mixture output layer (GMM); and a Bayesian Neural Network (BNN) with a GMM output layer. ANN estimates a single value of the photometric redshift z_{photo} . In contrast, the MDN and BNN models estimate the parameters of a GMM distribution, which yields a probability distribution of the photometric redshift $P(z_{\text{photo}})$. To enable a comparison between the ANN model and the MDN and BNN models, we obtain the point predictions z_{photo} from the MDN and BNN by taking the mean value of $P(z_{\text{photo}})$. We also evaluated the median and mode; however, the mean yielded the best performance in terms of mean squared error.

For the GMM and BNN, we vary the number of GMM components from one to five. All models utilize a series of fully connected layers with non-linear activation functions to map input features to the target space. The ANN is constructed with 11 hidden layers of 256 neurons each and produces a single scalar output as the final prediction. The MDNs employs an architecture consisting of 12 hidden layers with 512 neurons each. For MDN configurations utilizing multiple components, a dropout layer with a rate of 0.2 is integrated after every two hidden layers to improve generalization. The MDNs predict the parameters

of a GMM, returning a full probability density function that allows to capture of aleatoric uncertainty. We adopt the mean of this distribution as the point prediction and the standard deviation as the associated uncertainty.

The BNN also predicts GMM parameters through 12 hidden layers of 512 neurons; however, the final three layers are replaced with Flipout Bayesian layers. These layers treat weights as probability distributions, enabling the model to capture both aleatoric uncertainty via the mixture output and epistemic uncertainty through the weight distributions. BNN is intrinsically stochastic and yields a different prediction at each evaluation. We therefore generate 100 forward passes for each object. The final prediction is obtained by averaging the means of these draws. We quantify epistemic uncertainty as the variance of the 100 predicted means, while aleatoric uncertainty is estimated by averaging the predictive variances across the same draws. The total uncertainty is then calculated as the square root of the sum of the epistemic and aleatoric variances, ensuring the prediction and its uncertainty share the same physical units.

3.4. Model training

For the ANN model, we adopt the mean squared error (MSE) as the loss function, calculated on the residuals $\Delta z = z_{\text{photo}} - z_{\text{spec}}$, where z_{spec} is the spectroscopic redshift. We train all the remaining models using the negative log-likelihood (NLL) of the predicted distribution evaluated at the probability value given by the true z_{spec} . We optimize all networks using the Adaptive Moment Estimation (Adam, Kingma & Ba 2014), which utilizes adaptive learning rates. We use learning rate of 10^{-4} and apply early stopping, terminating training when the validation loss shows no improvement for 30 consecutive epochs. To prevent data leakage, we fit all normalization parameters (mean and variance) exclusively on the training set. We train each model five times and select, for the final evaluation, the realization that achieved the lowest loss on the validation set.

3.5. Model evaluation

To compare uncertainty models with simple ANN, we use:

- the mean squared error

$$\text{MSE} = \frac{1}{N} \sum (z_{\text{spec},i} - z_{\text{photo},i})^2, \quad (1)$$

- R-squared

$$R^2 = 1 - \frac{SS_{\text{RES}}}{SS_{\text{TOT}}} = 1 - \frac{(z_{\text{spec},i} - z_{\text{photo},i})^2}{(z_{\text{spec},i} - \bar{z}_{\text{spec}})^2}, \text{ and} \quad (2)$$

- the redshift error

$$\delta z = \frac{z_{\text{photo}} - z_{\text{spec}}}{1 + z_{\text{spec}}}, \quad (3)$$

where \bar{z}_{spec} is the mean spectroscopic redshift of a given validation sample. Since the ANN serves only as a baseline and the primary goal of this work is to assess uncertainty estimation, we adopt as our main evaluation metric the NLL of the predicted redshift distribution evaluated at z_{spec} , averaged over the different test sets. Unlike MSE, R^2 , and redshift error, the NLL evaluates the full predicted probability density function and therefore provides a direct measure of uncertainty quality.

To compare the total photo- z distribution predicted by each model with the spectroscopic redshift, we construct histograms

for both cases. We represent the spectroscopic distribution using a simple histogram of the reference redshifts $\Sigma(z_{\text{spec}})$. For the ML models, however, we account for the fact that the predictions take the form of probability density functions rather than point estimates.

We incorporate this probabilistic information through Monte Carlo sampling. For each object, we draw a single random sample from its predicted redshift distribution and construct a normalized histogram of the resulting sample. We repeat this procedure 5000 times and compute the mean histogram by averaging the counts in each bin. We adopt a bin width of $\delta z = 0.3$, which allows to focus on overall trends in redshift distributions. We select a large number of realizations to suppress Monte Carlo fluctuations and ensure convergence of the averaged histograms. We denote the resulting distribution as $\Sigma(P(z_{\text{photo}}))$.

To quantify the agreement between the photometric and spectroscopic redshift distributions, we compute the mean squared error:

$$\text{MSE}^* = \frac{10^3}{N} (\Sigma(z_{\text{spec}}) - \Sigma(P(z_{\text{photo}})))^T (\Sigma(z_{\text{spec}}) - \Sigma(P(z_{\text{photo}}))), \quad (4)$$

where N is the number of redshift bins, and 10^3 is a normalizing factor.

3.6. Unsupervised learning

In color space, a phenomenon known as photo- z degeneracy may occur, whereby two or more distinct redshift values correspond to the same set of feature values. In such cases, uncertainty-aware models may produce bimodal or multimodal predictions, resulting in multiple local maxima in the estimated photo- z distribution. To identify these degeneracies, we perform an analysis based on t-distributed stochastic neighbor embedding (t-SNE, van der Maaten & Hinton 2008) and hierarchical density based clustering (HDBSCAN, McInnes et al. 2017), applied to a feature space built from the PDFs of photo- z uncertainties.

For each object, the model outputs a full probability density function. We sample each $P(z_{\text{photo}})$ at 100 evenly spaced redshift values between $z = 0.05$ and $z = 5.0$, and we treat these sampled probability values as a feature vector for further analysis. To visualize this high-dimensional feature space, we reduce its dimensionality to two using t-SNE. t-SNE is a non-linear dimensionality reduction technique designed to preserve the local structure of high-dimensional data in a low-dimensional map. To ensure that objects are grouped based on the similarity of their $P(z_{\text{photo}})$ shapes rather than absolute values, we utilized correlation distance as the metric for the embedding. We configure the algorithm with a perplexity of 40 and a learning rate of 200 to ensure stable convergence and a clear representation of the global manifold.

We subsequently apply the HDBSCAN to the embedded representations, with the minimum cluster size set to 50, and 5 samples required to form a core point. HDBSCAN is a density-based clustering tool that identifies groups of points closely packed together, while marking points in sparse regions as noise. Unlike K-Means, it automatically determines the number of clusters based on the data density structure. For each identified cluster, we construct a total redshift distribution histogram in order to examine the characteristic shape of the predicted distribution within that cluster.

4. Results

4.1. Model performance

Table 1. Comparison of point estimates for quasars in random test set with complete features. The point estimates are defined as mean values of estimated photo- z probability distributions.

network	# GMM	MSE	R ²	δz
ANN	0	0.092	0.811	0.014 ± 0.135
MDN	1	0.084	0.827	$\mathbf{0.004} \pm 0.123$
	2	0.076	0.845	$0.012 \pm \mathbf{0.119}$
	3	0.077	0.841	0.013 ± 0.123
BNN	3	0.076	0.843	0.015 ± 0.123

We first evaluate point photo- z predictions, followed by individual uncertainty estimates. In the next Section, we present the redshift distributions. Table 1 summarizes the metrics computed from single-value photo- z predictions for a random test set with complete features. We find that incorporating uncertainty predictions leads to improved performance relative to the ANN model. According to the MSE, R², and δz metrics, the MDN model with at least two GMM components, as well as the BNN model with three GMM components, achieve the best results. However, these metrics do not assess the full photo- z probability distributions and therefore do not allow us to identify the best-performing model among the photo- z uncertainty estimation approaches.

When evaluating photo- z uncertainties, adding the second and third GMM components reduces the NLL, where a lower value indicates a better fit (Table 2). Models with four and five components do not yield further improvement. In the faint-extrapolation test with complete features, the performance improve with each additional component up to four, while the five-component model exhibits a degradation. The performance decreases for subsets containing missing features; however, the relative ranking of the models remains similar.

The BNN achieves the lowest NLL in all three tests when additional sources of uncertainty are included. A direct comparison between the best-performing MDN and BNN models, both with three GMM components, shows that the BNN performs worse by +0.07 in NLL relative to the MDN on the random test set with complete features, but improves the NLL by -0.11 on the faint-extrapolation test set with complete features. For the datasets with missing features, these differences amount to -0.13 and -0.05, respectively, both in favor of the BNN.

4.2. Redshift distribution

Fig. 2 presents the results of the redshift distribution reconstruction under four test scenarios. We compare our predictions (black) with the underlying true spectroscopic distributions (red). In the first row, corresponding to the complete dataset with full magnitude coverage, the ANN model without uncertainty estimation yields an MSE* value 6 times larger than that of the best-performing MDN model with three mixture components (MDN 3). The ANN reconstruction additionally exhibits pronounced step-like features in the recovered distribution, reflecting a preference for discrete photo- z predictions—an effect absent in models that explicitly estimate photo- z uncertainties. The MDN 3 achieves three times better MSE* than MDN 1. Among the uncertainty-aware models, the BNN provides a better fit to the true distribution than the MDN.

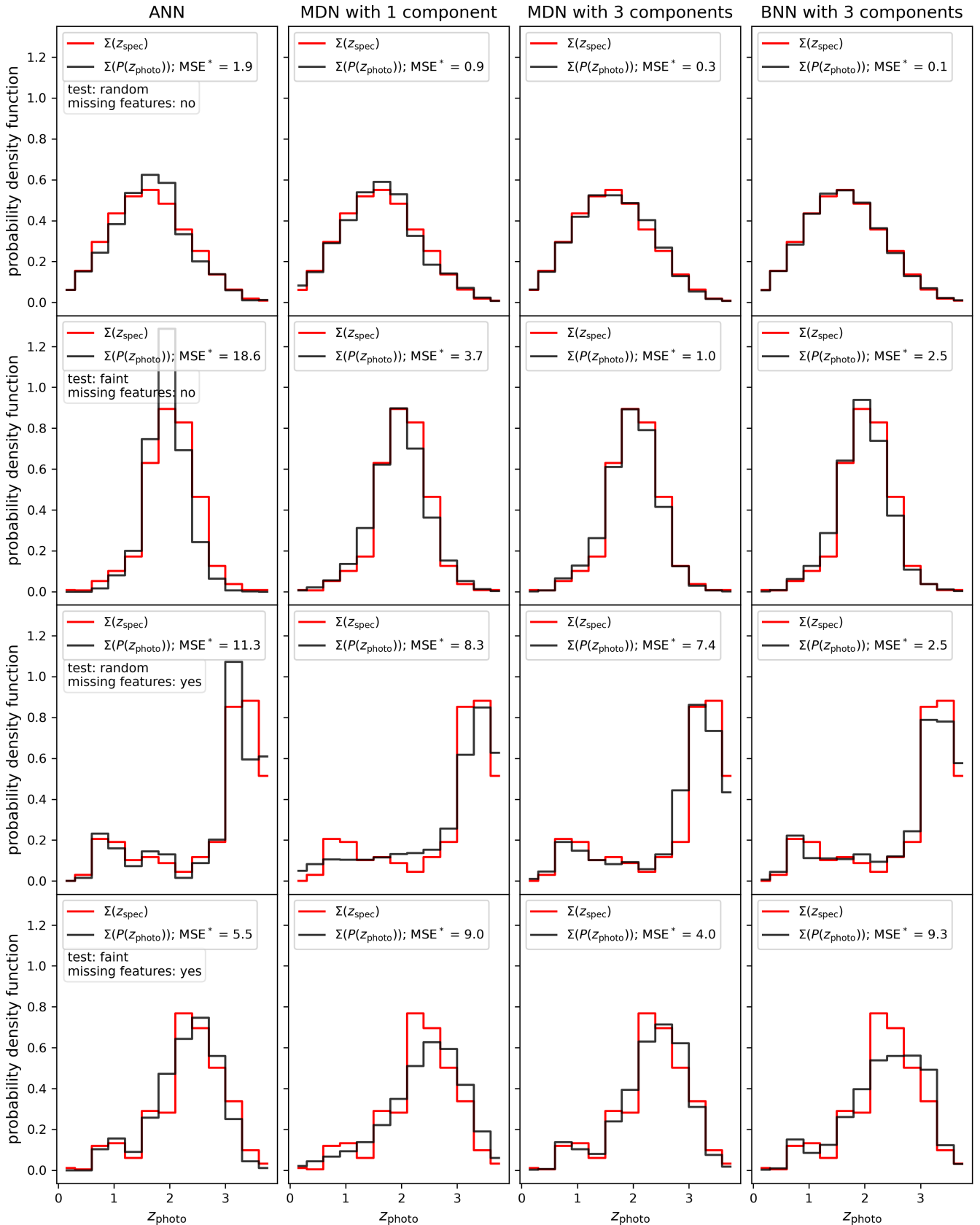


Fig. 2. Spectroscopic (red) and photo- z (black) redshift distributions for ANN (column 1), MDN with 1 mixture component (column 2), MDN with 3 mixture components (column 3), and BNN with 3 mixture components (column 4). Histograms correspond to four subsets: random test data with complete features (row 1), random test data with at least one missing feature (row 2), faint-extrapolation test data with complete features (row 3), and faint-extrapolation test data with at least one missing feature (row 4). We compute the mean squared error multiplied by a factor of 10^3 (MSE^*) for each model with respect to the spectroscopic distributions.

Table 2. Comparison of negative log-likelihood (NLL) for MDN with varying numbers of mixture components and a BNN with three components. We evaluate each model four subsets: complete features in random test; complete features in faint-extrapolation test; at least one missing feature in random test; at least one missing feature in faint-extrapolation test.

network	#GMM	complete features		missing features	
		random test	faint test	random test	faint test
MDN	1	-0.19	0.68	0.44	1.28
	2	-0.68	0.45	0.11	1.03
	3	-0.69	0.25	0.07	0.74
	4	-0.68	0.18	0.12	0.75
	5	-0.69	0.26	0.05	0.77
BNN	3	-0.62	0.14	-0.06	0.69

In the second row, corresponding to the extrapolation test with all magnitudes available, the performance degrades relative to the complete test: the MSE^* increases by a factor of 3 for MDN 3, and 25 for BNN 3. Once again, MDN 3 and BNN 3 provide the most accurate reconstructions of the distribution; however, in this case, MDN 3 achieves the lower MSE^* .

For the tests with missing features, the RSS values are substantially worse. In the random test (row 3), BNN 3 achieves the lowest MSE^* . The fourth row represents the most challenging scenario, combining extrapolation with missing magnitudes, where MDN 3 again attains the best performance.

Based on these comparisons, we define the following MSE^* values:

$MSE^* < 0.5$ – accurate reconstruction,
 $0.5 < MSE^* < 1.5$ – minor distortions,
 $1.5 < MSE^* < 2.5$ – significant biases,
 $2.5 < MSE^*$ – failure of reconstruction.

According to these ranges, the reconstruction is accurate for high-quality data in the first row, exhibits minor distortions in the case of extrapolation, shows significant bias when features are missing, and fails when both sources of measurement uncertainty occur simultaneously. It highlights a significant limitation of all approaches under simultaneously incomplete and out-of-distribution conditions.

4.3. Degeneracies

Fig. 3 shows the t-SNE projections of photo- z PDFs. We restrict this analysis to the random test set without missing features and to the MDN with three components. The global structure resembles a spiral with several additional clusters. Objects for which the model predicts similar redshift values clearly cluster next to each other, forming a smooth gradient along the spiral: lower redshift values occupy the upper part of the spiral, while higher values appear toward the bottom. The distribution of standard deviation values remains relatively flat and shows comparable levels across most regions of the projection; the main exceptions correspond to clusters 5, 8 and -1, where the uncertainties increase noticeably. Cluster -1 usually represents outliers, while in our case it corresponds to the smallest cluster.

To characterize the objects within each cluster in more detail, we construct photo- z histograms of all objects in each cluster (Fig. 4). Among the clusters identified as suspicious, clusters 8 and -1 exhibits clear signs of degeneracy. While a similar histogram shape could result from objects with single-peaked distributions at different redshifts, the objects in cluster 8 share comparable predicted redshift values, indicating genuine multimodality. Cluster 5 does not show such behavior. The degenerate redshift pairs are (1.2, 2.3) for cluster 8 and (1.6, 2.5) for cluster -1. The sizes of clusters 8 and -1 are 0.5% and 0.2%,

respectively. We note that the full KiDS data, which is the final target for photo- z inference, contains a higher fraction of faint objects than the sample analyzed here. The increased noise associated with these fainter sources may, in turn, lead to a higher incidence of degenerate predictions.

We examine whether cluster 8 could be characterized by specific features that would explain its degeneracy, but find no clear distinguishing properties. This suggests that, in the absence of sufficiently informative features, the model may express uncertainty through multi-peaked photo- z estimates.

5. Conclusions

In this work, we perform a comprehensive comparison of photometric redshift (photo- z) uncertainty estimation methods using machine learning techniques applied to quasars. We also assess the impact of photo- z uncertainty on the reconstruction of the underlying redshift distribution. We provide a quantitative comparison and practical guidelines for addressing photo- z prediction across a range of data quality scenarios and domain shifts. Our analysis is based on photometric observations from the KiDS combined with spectroscopically confirmed quasars from DESI, enabling a controlled evaluation under well-defined training conditions.

We demonstrate that an accurate reconstruction of the true redshift distribution is fundamentally unattainable without a robust uncertainty estimation framework. In particular, Mixture Density Networks (MDN) with at least two components are essential to capture the intrinsic multi-modality of photo- z solutions. Among the MDN models, an MDN with three Gaussian Mixture Model (GMM) components consistently provides the best overall performance across reconstruction accuracy and likelihood-based metrics.

Bayesian neural networks (BNNs) exhibit clear advantages in extrapolative regimes, where inference data extend beyond the magnitude range covered by the training set. In such cases, BNNs improve the negative log-likelihood by 0.11 over MDN, indicating a more realistic uncertainty quantification. However, this benefit comes at the cost of reduced performance for well-covered, brighter sources, where an increase in NLL of 0.07 is observed. This trade-off highlights the context-dependent nature of Bayesian approaches in photo- z estimation.

We find that redshift distribution reconstruction is highly accurate when inference data are complete and well represented in the training set. Moderate reconstruction errors emerge in scenarios involving either feature incompleteness or extrapolation beyond the training magnitude range, while the simultaneous presence of both effects leads to substantial degradation in reconstruction quality. These results emphasize the compounded

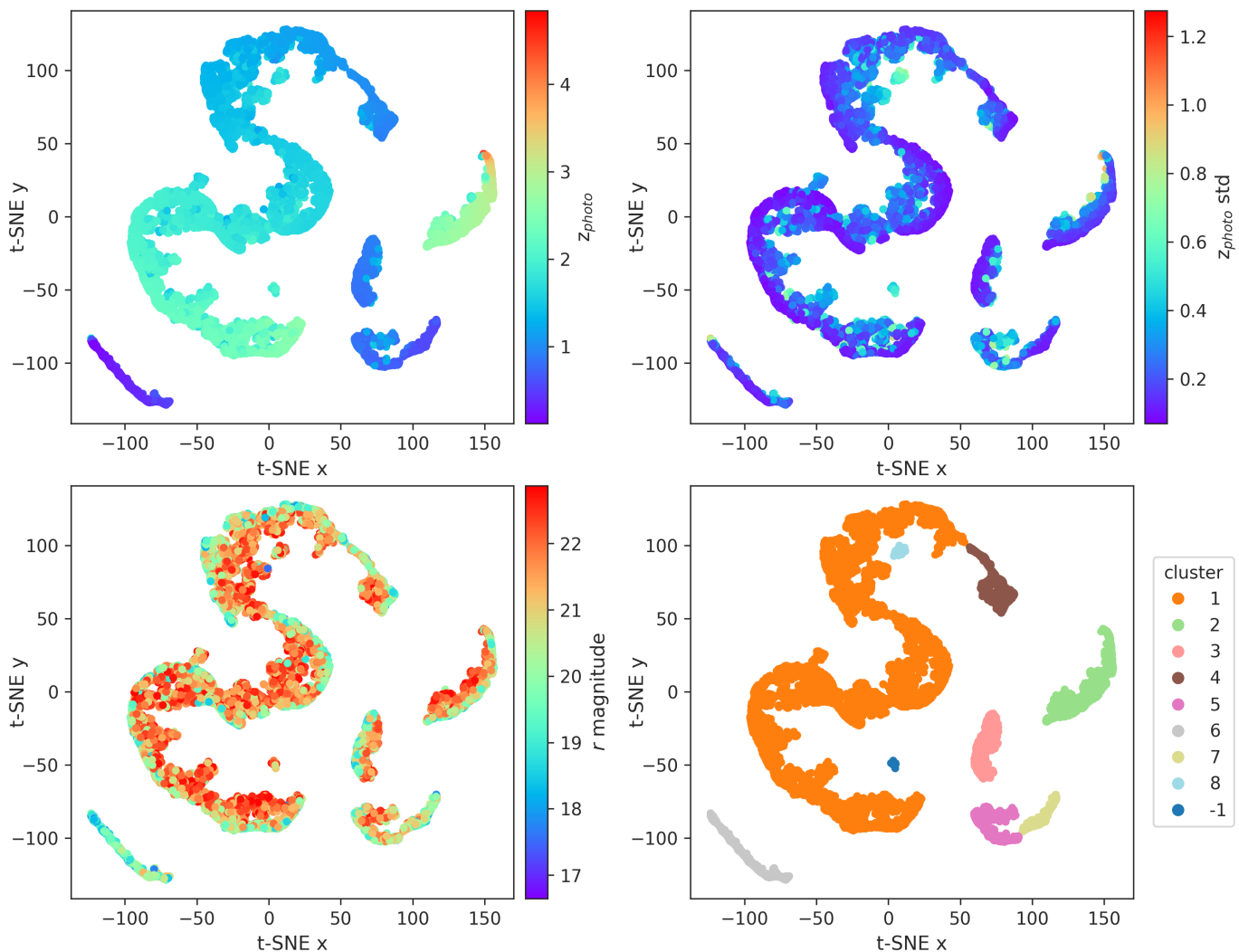


Fig. 3. t-SNE projection of photo- z estimates in the random test data with complete features. *Top-left:* mean photo- z , *top-right:* photo- z standard deviation, *bottom-left:* r magnitude, *bottom-right:* clusters. For each object, we use an array of equally spaced 100 probability density function (PDF) values calculated from model output.

impact of data incompleteness and domain shift on cosmological inference.

Furthermore, our unsupervised clustering analysis reveals two distinct clusters associated with degeneracies between two competing redshift solutions, at redshift pairs of (1.2, 2.3) and (1.6, 2.5). The unsupervised clustering of photo- z predictions proves to be an efficient and insightful diagnostic tool for identifying such degeneracies, offering a complementary perspective on uncertainty beyond traditional scalar metrics. The identified degeneracy may lead to incorrect assignment of objects to bins during tomographic analysis. Our methodology provides an easy framework to remove the degenerated objects from the cosmological inference. Developing a method to resolve this degeneracy could provide the most effective pathway toward improving quasar photo- z estimation.

One of the issues not addressed in detail in this work is the impact of missing magnitudes on the photo- z results. In our approach, we group all objects with missing magnitudes into a single subset; however, given that different photometric bands contribute unequally to photo- z estimation, it would be advisable to

perform this analysis separately for different patterns of missing magnitudes.

It is important to note that this study is based on training data drawn from the overlap between the KiDS and DESI surveys, and therefore does not explicitly probe the additional effects of training–inference domain mismatch. As a result, our findings should be interpreted as an upper bound on achievable photo- z performance. Future studies could investigate the impact of removing objects with the largest photo- z uncertainties on the reconstructed redshift distribution, as well as explore approximate Bayesian techniques such as Monte Carlo dropout, which are widely adopted in deep learning applications.

The findings of this work are particularly relevant for forthcoming large-scale surveys such as *Euclid* (Euclid Collaboration et al. 2022), the Legacy Survey of Space and Time (LSST, Ivezić et al. 2019), and the Nancy Grace Roman Space Telescope (Green et al. 2012), where photo- z estimation will be a critical systematic for cosmological analyses. These surveys will rely heavily on precise reconstruction of redshift distributions for weak lensing, galaxy clustering, and cross-correlation studies, often in regimes where training

data are incomplete or not fully representative. The guidelines and quantitative comparisons presented here provide a practical framework for selecting and validating photo- z uncertainty methods, as well as removing photo- z degeneracies, in these next-generation cosmological experiments. In essence, better understanding how uncertain our redshift estimates are brings us one step closer to mapping the Universe with confidence rather than guesswork.

Acknowledgements. We would like to thank Hendrik Hildebrandt for valuable discussions and for providing an internal review of this work. SJN and MB are supported by the Polish National Science Center through grant no. 2020/38/E/ST9/00395. Based on data obtained from the ESO Science Archive Facility with DOI: <https://doi.org/10.18727/archive/37>, and <https://doi.eso.org/10.18727/archive/59> and on data products produced by the KiDS consortium. The KiDS production team acknowledges support from: Deutsche Forschungsgemeinschaft, ERC, NOVA and NWO-M grants; Target; the University of Padova, and the University Federico II (Naples). The following software was used: Python 3 (Van Rossum & Drake 2009), TensorFlow (Abadi et al. 2015), Keras (Chollet 2015), Scikit-learn (Pedregosa et al. 2011), NumPy (Harris et al. 2020), SciPy (Virtanen et al. 2020), IPython (Pérez & Granger 2007), Pandas (Wes McKinney 2010), Matplotlib (Hunter 2007), seaborn (Waskom 2021), tqdm (da Costa-Luis 2019).

References

- Abadi, M., Agarwal, A., Barham, P., et al. 2015, TensorFlow: Large-Scale Machine Learning on Heterogeneous Systems, software available from tensorflow.org
- Alonso, D., Bellini, E., Hale, C., Jarvis, M. J., & Schwarz, D. J. 2021, MNRAS, 502, 876
- Bilicki, M., Dvornik, A., Hoekstra, H., et al. 2021, A&A, 653, A82
- Chen, J., Luo, Z., Fu, L., et al. 2025, arXiv e-prints, arXiv:2512.16010
- Chollet, F. 2015, keras, <https://github.com/fchollet/keras>
- da Costa-Luis, C. 2019, The Journal of Open Source Software, 4, 1277
- DESI Collaboration, Aghamousa, A., Aguilar, J., et al. 2016, arXiv e-prints, arXiv:1611.00036
- DESI Collaboration, Karim, M. A., Adame, A. G., et al. 2025, arXiv e-prints, arXiv:2503.14745
- D’Isanto, A. & Polsterer, K. L. 2018, A&A, 609, A111
- Edge, A., Sutherland, W., Kuijken, K., et al. 2013, The Messenger, 154, 32
- Eltvedt, A. M., Shanks, T., Metcalfe, N., et al. 2024, MNRAS, 535, 2105
- Euclid Collaboration, Scaramella, R., Amiaux, J., et al. 2022, A&A, 662, A112
- Green, J., Schechter, P., Baltay, C., et al. 2012, arXiv e-prints, arXiv:1208.4012
- Harris, C. R., Millman, K. J., van der Walt, S. J., et al. 2020, Nature, 585, 357
- Hildebrandt, H., Arnouts, S., Capak, P., et al. 2010, A&A, 523, A31
- Hildebrandt, H., van den Busch, J. L., Wright, A. H., et al. 2021, A&A, 647, A124
- Hunter, J. D. 2007, Computing in Science & Engineering, 9, 90
- Ivezić, Ž., Kahn, S. M., Tyson, J. A., et al. 2019, ApJ, 873, 111
- John William, A., Bilicki, M., Hellwing, W. A., Nakoneczny, S. J., & Jalan, P. 2025a, arXiv e-prints, arXiv:2511.17311
- John William, A., Jalan, P., Bilicki, M., et al. 2025b, A&A, 698, A276
- Jones, E., Do, T., Boscoe, B., et al. 2024, ApJ, 964, 130
- Kingma, D. P. & Ba, J. 2014, arXiv preprint arXiv:1412.6980
- Kuijken, K. 2008, A&A, 482, 1053
- Kuijken, K., Heymans, C., Dvornik, A., et al. 2019, A&A, 625, A2
- Kuijken, K., Heymans, C., Hildebrandt, H., et al. 2015, MNRAS, 454, 3500
- Li, R., Napolitano, N. R., Feng, H., et al. 2022, A&A, 666, A85
- Luo, Z., Li, Y., Lu, J., et al. 2024, MNRAS, 535, 1844
- McInnes, L., Healy, J., & Astels, S. 2017, Journal of Open Source Software, 2, 205
- Nakoneczny, S. J., Alonso, D., Bilicki, M., et al. 2024, A&A, 681, A105
- Nakoneczny, S. J., Bilicki, M., Pollo, A., et al. 2021, A&A, 649, A81
- Newman, J. A. & Gruen, D. 2022, ARA&A, 60, 363
- Pasquet, J., Bertin, E., Treyer, M., Arnouts, S., & Fouchez, D. 2019, A&A, 621, A26
- Pedregosa, F., Varoquaux, G., Gramfort, A., et al. 2011, Journal of Machine Learning Research, 12, 2825
- Pérez, F. & Granger, B. E. 2007, Computing in Science and Engineering, 9, 21
- Petter, G. C., Hickox, R. C., Alexander, D. M., et al. 2023, ApJ, 946, 27
- Salvato, M., Ilbert, O., & Hoyle, B. 2019, Nature Astronomy, 3, 212
- Vakili, M., Hoekstra, H., Bilicki, M., et al. 2023, A&A, 675, A202
- van der Maaten, L. & Hinton, G. 2008, Journal of Machine Learning Research, 9, 2579
- Van Rossum, G. & Drake, F. L. 2009, Python 3 Reference Manual (Scotts Valley, CA: CreateSpace)
- Virtanen, P., Gommers, R., Oliphant, T. E., et al. 2020, Nature Methods, 17, 261
- Waskom, M. L. 2021, Journal of Open Source Software, 6, 3021
- Wes McKinney. 2010, in Proceedings of the 9th Python in Science Conference, ed. Stéfan van der Walt & Jarrod Millman, 56 – 61
- Wright, A. H., Kuijken, K., Hildebrandt, H., et al. 2024, A&A, 686, A170
- Zhang, C., Wang, W., Qu, M., Jiang, B., & Zhang, Y. 2024, AJ, 168, 244
- Zhou, X., Gong, Y., Meng, X.-M., et al. 2022, Research in Astronomy and Astrophysics, 22, 115017

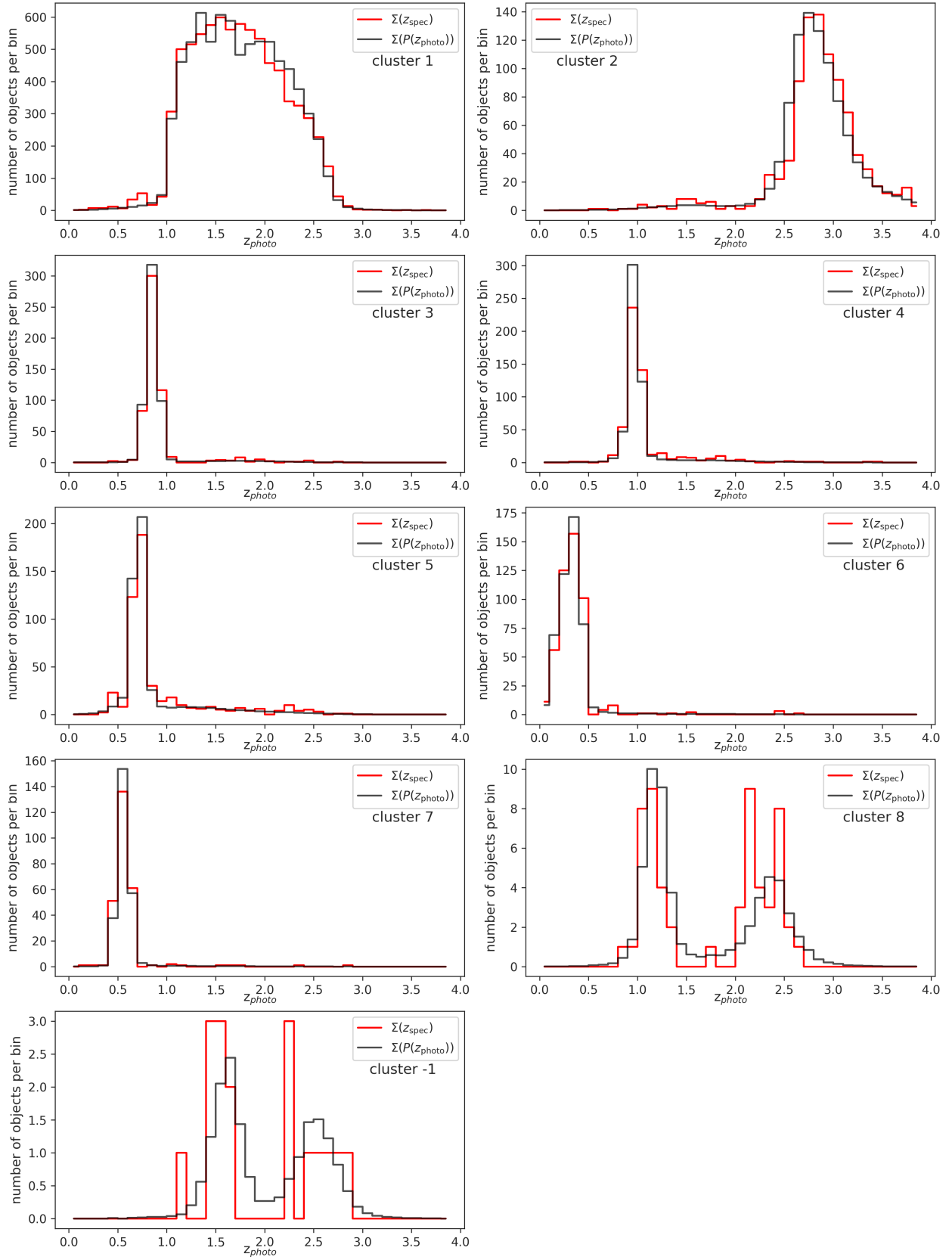


Fig. 4. Spectroscopic and photometric redshift distributions for all clusters.